ELSEVIER

Journal of Chromatography A, 890 (2000) 321–336

JOURNAL OF CHROMATOGRAPHY A

www.elsevier.com/locate/chroma

Simulation of electrophoretic separations by the flux-corrected transport method

T.L. Sounart, J.C. Baygents*

Department of Chemical and Environmental Engineering, The University of Arizona, Tucson, AZ 85721, USA

Received 5 January 2000; received in revised form 30 March 2000; accepted 18 April 2000

Abstract

Electrophoretic separations at typical experimental electric field strengths have been simulated by applying the flux-corrected transport (FCT) finite difference method to the transient, one-dimensional electrophoresis model. The performance of FCT on simulations of zone electrophoresis (ZE), isotachophoresis (ITP), and isoelectric focusing (IEF) has been evaluated. An FCT algorithm, with a three-point, central spatial discretization, yields numerical solutions without numerical oscillations or spurious peaks, which have plagued previously-published second-order solutions to benchmark ZE and ITP problems. Moreover, the FCT technique captures sharp zone boundaries and IEF peaks more accurately than previously-published, first-order upwind schemes.

Keywords: Flux-corrected transport; Computer simulation; Electric field strength

1. Introduction

Electrophoretic separations encompass a variety of well-established techniques for fractionating mixtures of ionic solutes for analytical and preparative applications. The desire to enhance separation efficiencies, resolution, and sensitivity continues to spur the development of new and improved methods. For example, lab-on-a-chip technology has introduced a new approach to electrophoretic separations, and underscored the need for a more refined understanding of electromigrational transport processes [1]. Computer simulations have the potential to play a vital role in the development of new separations by providing a tool to explore the effects of various operating parameters. Simulations also afford the opportunity to examine processes, such as the evolution of the concentration, fluid velocity, electric, and conductivity fields, which are not amenable to experimental investigation in microscale systems. However, the potential utility of numerical simulations has not been completely realized inasmuch as many problems of interest are not yet tractable.

A general set of balance laws for electrophoretic separations was first introduced by Bier and coworkers [2], who developed a computer simulation of the classical modes of electrophoretic separation [3–5]. Dose and Guiochon [6] subsequently reduced computation times by introducing column segmentation to eliminate repetitious calculations in regions where the first and second spatial derivatives of all components vanished. Schafer-Nielsen [7] recognized that for separations involving weak electrolytes, most of the computation time was devoted

*Corresponding author. Tel.: +1-520-621-6043; fax: +1-520-621-6048.

E-mail address: jcb@maxwell.che.arizona.edu (J.C. Baygents).

0021-9673/00/$ – see front matter
PII: S0021-9673(00)00500-8

to solving the nonlinear set of algebraic equations required to evaluate the pH and ionic speciation; computation efficiency was improved by eliminating this calculation where and when all component concentrations remained constant. These early and other similar schemes [8] were suited to nominal electric field strengths approximately two orders of magnitude lower than those now typically used in practice (50–500 V/cm). Their high-field deficiencies result from the accumulation of substantial discretization errors introduced in regions of sharp concentration gradients by higher-order (order 2 and above) finite difference approximations. These discretization errors accumulate to form artifactual peaks or valleys which spawn additional peaks and valleys, and perpetuate the growth of spurious oscillations.

Ermakov et al. [9,10] controlled the numerical oscillations by adding artificial dispersion terms to the discretized equations, and hence were able to simulate zone electrophoresis (ZE) and isotachophoresis (ITP) at higher electric field strengths. This method, though a substantial improvement over previous numerical implementations, still failed to suppress oscillations in simulations with local field strengths of $O(100$ V/cm). Martens et al. [11] evaluated the application of several implicit upwind numerical methods, including first and higher-order schemes, to the simulation of ZE and ITP separations. The higher-order schemes exhibited numerical oscillations and/or significant mass balance errors. The first-order upwind schemes suppressed all oscillations without significant mass balance errors, but included numerical diffusion that resulted in overprediction of zone boundary thicknesses. Ikuta and Hirokawa [12] simulated high-field ZE with an explicit first-order upwind method that proved to be numerically monotonic but also suffered from numerical diffusion. Application of these high-field methods to the simulation of isoelectric focusing (IEF) has not been reported.

Development of higher-order finite difference methods for solving advection problems involving sharp gradients began in the early 1970s with the use of flux limiters [13–15]. Van Leer [14] and Boris and Book [15] independently introduced the first flux limiter methods, and development of these and related methods has continued over the last three decades. The flux-corrected transport (FCT) method originated by Boris and Book was initially developed for hyperbolic conservation laws [15–21], and is an appealing method because it is both monotonic and second-order accurate. FCT algorithms are multi-step finite difference schemes in which numerical diffusion is included in a higher-order finite difference representation of the conservation law; this prevents spurious peak formation. The numerical diffusion is then removed in a subsequent 'antidiffusion' step, except from regions where it is needed to offset the discretization error that would otherwise lead to spurious peak development. An antidiffusion-flux limiter is used to decide where and how much of the numerical diffusion should be removed. Successful implementations of FCT have been demonstrated for various higher-order schemes, numerical diffusion and antidiffusion coefficients, antidiffusion flux limiters, etc. [16–23]. In the specific context of electrophoresis, Clifton [24] and Blanco et al. [25] respectively applied an FCT algorithm to a steady-state, continuous-flow (CFE) model and to high-field protein ZE.

In this paper we examine FCT as a general high-field method to simulate the various modes of electrophoretic separation, and compare the technique to more conventional approaches (i.e. no flux limiter). We adapt the Boris and Book approach to the parabolic conservation laws of the transient electrophoresis model and preserve the essential aspects of FCT, viz., spurious oscillations are suppressed and numerical diffusion is controlled. The effectiveness of any numerical approach can vary dramatically with the physics of the problem, and ITP and IEF differ mechanistically from ZE and CFE. Thus, to evaluate the broad performance of the FCT algorithm, we simulate three benchmark electrophoretic separations–a ZE, an ITP, and an IEF separation–at realistic electric field strengths. The ZE and ITP benchmarks have been used previously by others to evaluate various numerical schemes [10–12]. For comparison, the separations are also simulated using two other common explicit finite difference methods: a first-order explicit upwind scheme and the second-order central difference scheme employed by Palusinski et al. [4]. The spatial discretization of the upwind scheme is equivalent to the Diffusion Implicit Migration Explicit (DIME)

scheme described by Martens et al. [11], except the diffusion term is treated explicitly rather than implicitly. The FCT solutions converged on significantly coarser grids than did the upwind and central difference solutions, and FCT provided substantially more accurate solutions to the electrophoresis model when compared on the same grid. For example, FCT simulations of IEF were non-oscillatory on spatial grids where the explicit upwind scheme exhibited significant mass balance errors, and where the central difference scheme was either oscillatory or unstable. In contrast to the numerical method described by Ermakov et al. [10], the FCT simulations showed no spurious oscillations on any spatial grid, and sharp zone boundaries were captured more faithfully than by the first-order upwind schemes described by Martens et al. [11] and by Ikuta and Hirokawa [12]. As a result, FCT solutions provided information on the benchmark separations that could not be obtained by the previously-published simulations [10–12].

2. Balance laws for electrophoretic separations

A general set of balance laws, governing the transport of ionic and neutral compounds in isothermal electrophoretic separations, was developed in the 1980s [2–4], and later detailed in a monograph by Mosher et al. [5]. This coupled set of nonlinear partial differential and algebraic equations includes an unsteady electromigration–diffusion equation for each solutal component, a charge balance, the electroneutrality approximation, expressions for ionogenic dissociation–association equilibria, and a model for calculating protein mobilities as a function of pH and ionic strength. The balance laws are summarized here in a form suited to FCT simulations. A notation similar to that introduced by Clifton [25] is used.

Ion concentrations, pH, and effective valences are determined by a coupled set of mass–action relations. These include the dissociation of water, viz.

$$K_w \equiv [H^+][OH^-] = 10^{-14} M^2 \tag{1}$$

and the ion dissociation–association equilibria for M solutal components. If the neutral form of the kth component A_k^0 is protonated or deprotonated to form P_k cationic and N_k anionic species, then the mass action relations for ions of valence z are

$$A_k^z \rightleftharpoons H^+ + A_k^{z-1},$$
$$\begin{cases} z = -N_k + 1, -N_k + 2, \ldots, +P_k \\ k = 1, 2, \ldots, M, \end{cases}$$

which are characterized by the equilibrium constants

$$K_k^z \equiv \frac{[H^+] n_k^{z-1}}{n_k^z},$$
$$\begin{cases} z = -N_k + 1, -N_k + 2, \ldots, +P_k \\ k = 1, 2, \ldots, M, \end{cases} \tag{2}$$

where n_k^z is the concentration of subspecies A_k^z. It follows from the electroneutrality approximation that

$$0 = \sum_{k=1}^{M} \bar{z}_k C_k + [H^+] - \frac{K_w}{[H^+]}, \tag{3}$$

where C_k is the concentration and $\bar{z}_k$ is the effective valence of the kth component, i.e.

$$C_k \equiv \sum_{z=-N_k}^{+P_k} n_k^z, \quad k = 1, 2, \ldots, M, \tag{4}$$

and

$$\bar{z}_k \equiv \frac{\sum_{z=-N_k}^{+P_k} z n_k^z}{C_k}, \quad k = 1, 2, \ldots, M. \tag{5}$$

To account for local variations of the C_k, a mass balance is written for each component,[1] viz.

$$\frac{\partial C_k}{\partial t} = -\nabla \cdot [\mathbf{v}_k^e C_k - \omega_k k_B T \nabla C_k],$$
$$k = 1, 2, \ldots, M, \tag{6}$$

and this forms a set of non-linear electro-diffusional transport equations, coupled through the electric field and the component speciation. In Eqs. (6), $k_B T$ is the Boltzmann temperature, and ω_k is the hydrodynamic mobility of the kth component (taken here to be independent of component speciation); $\mathbf{v}_k^e$ is the effective component electrophoretic velocity, viz.

[1] The local fluid velocity is not included in this formulation, but a uniform fluid velocity field (such as the mean electroosmotic flow [26,27]) can be accommodated by adopting a frame of reference moving with the fluid velocity.

$$\mathbf{v}_k^e = e\bar{z}_k\omega_k\mathbf{E}, \quad k = 1, 2, \ldots, M, \tag{7}$$

where **E** is the local electric field, and e is the charge on a proton (1.6×10^{-19} C).

The governing equations are closed by combining Eqs. (3) and (6) to balance the charge; this yields an equation for **E**, i.e.

$$0 = \nabla\cdot\left[\sigma\mathbf{E} + ek_BT\left(\sum_{k=1}^{M}\omega_k\nabla\bar{z}_kC_k + \omega_H\nabla[H^+] - \omega_{OH}K_w\nabla[H^+]^{-1}\right)\right], \tag{8}$$

where

$$\sigma = e^2\left[\sum_{k=1}^{M}\bar{z}_k^2\omega_kC_k + \omega_H[H^+] + \omega_{OH}\frac{K_w}{[H^+]}\right] \tag{9}$$

is the local electrical conductivity. In Eqs. (8) and (9), ω_H and ω_{OH} are, respectively, the hydrodynamic mobilities of H^+ and OH^-, and $\bar{z}_k^2$ is the mean square valence of the kth component, viz.

$$\bar{z}_k^2 \equiv \frac{\sum_{z=-N_k}^{+P_k} z^2n_k^z}{C_k}, \quad k = 1, 2, \ldots, M. \tag{10}$$

For components that may undergo many protonation or deprotonation reactions (e.g. proteins), dissociation–association equilibrium constants are not necessarily available. In such cases, subspecies concentrations are not calculated, and effective and mean square valences are extracted from titration data. For details on the calculation of effective and mean square valences from titration data, and the calculation of protein mobilities as a function of pH and ionic strength, see Mosher et al. [5].

3. Numerical implementation

Standard numerical techniques, when applied to Eqs. (6), and implemented for typical experimental conditions, evince gross instabilities or inefficiencies. The numerical problems arise as the potential gradients exceed 10 V/cm. Electromigrational (or electrophoretic) transport of the ionic solutes dominates diffusion, and the unsteady electro-diffusional transport equations (Eqs. 6) approach a hyperbolic form. As a result, linear finite difference schemes, with second-order and higher spatial accuracy, yield solutions with numerical overshoots, undershoots, or oscillations in the vicinity of sharp concentration gradients (unless an impractically fine mesh is applied). To guarantee numerical monotonicity, a one-dimensional central spatial discretization of Eqs. (6), such as that employed by Palusinski et al. [4] and by Dose and Guiochon [6], requires that

$$Pe_{\Delta x} \equiv \frac{|v^e|\Delta x}{D} < 2 \tag{11}$$

for each component at all times and positions. In (11), $Pe_{\Delta x}$ is the cell electric Peclet number and Δx is the spatial grid size; D is the diffusivity and $|v^e|$ is the magnitude of the local electrophoretic velocity of the component. To satisfy (11), the number of segments n_s in a discretized domain of length L, must vary as $n_s \sim (Pe_{\Delta x})_{max}\ L/\Delta x \equiv Pe_L$ for a fixed uniform grid. Potential gradients exceeding 10 V/cm typically correspond to $Pe_L > O(10^3)$, and this dictates an impractical $n_s > O(10^3)$ to guarantee monotonic simulations. Ermakov et al. [9,10] developed a numerical scheme employing artificial dispersion, which greatly improved the simple central difference methods. Unfortunately, this method produced oscillatory solutions when simulating electrophoretic separations with $Pe_L > O(10^4)$.

Some first-order finite difference schemes, on the other hand, such as the upwind schemes described by Martens et al. [11] and by Ikuta and Hirokawa [12], are monotonic at any $Pe_{\Delta x}$ but suffer from excessive numerical diffusion. The lower accuracy of these schemes is generally considered more tolerable than the spurious peaks and distorted concentration profiles generated by the higher-order difference methods. Though the first-order upwind difference methods yield monotonic solutions for any grid spacing, they require an extremely fine mesh to substantially reduce numerical diffusion, and the resultant n_s is comparable to that required of the central difference schemes to maintain $Pe_{\Delta x} < 2$.

Since these numerical difficulties arise when electromigration dominates the electro-diffusional transport of solutes, it seems reasonable to consider the use of numerical methods developed for solving hyperbolic partial differential equations. There is a

class of such methods that apply flux or slope limiters [13] to higher-order difference schemes to prevent the formation of spurious overshoots or undershoots. The limiter is basically a set of rules designed to recognize the formation of a numerical undershoot or overshoot, and to remove it or prevent its formation by limiting the fluxes in these regions. This is done while maintaining a higher-order accurate finite difference approximation throughout the remainder of the simulation domain. Distinct sets of rules, and methods of implementing them, differentiate the various flux limiter methods.

The flux-limiter method of Boris and Book (FCT) employs a multi-step process in which sufficient numerical diffusion is added to a higher-order finite difference solution to ensure monotonicity [15–21]. The numerical diffusion is then removed in an antidiffusion step except where the antidiffusion fluxes are limited by a set of rules to prevent the formation of numerical overshoots or undershoots. Because the FCT method was formulated to yield monotonic solutions to unsteady hyperbolic equations, there is no limit on $Pe_{\Delta x}$ when applying FCT to unsteady advection–diffusion (or electromigration–diffusion) equations [15–21].

3.1. PLPE FCT

In simple tests on unsteady convection problems, an FCT algorithm called Shasta Phoenical Low Phase Error performed the best of the explicit methods evaluated by Boris and Book [17]. They and co-workers later applied the phoenical low phase error (PLPE) approach to a second-order central spatial discretization and incorporated the algorithm into several library subroutines [18,19,21]. Since this method employs a second-order central difference spatial discretization, it is a natural choice for modifying the numerical implementation of the electrophoresis model developed by Palusinski et al. [4].

The PLPE FCT method was applied to Eqs. (6) in one space dimension using a second-order Runge–Kutta (RK) time step and central difference spatial discretization, thus creating a scheme which is of second order in both time and space except in the regions where the nonlinear flux correction makes it impossible to determine the order of the truncation error. Eqs. (6) were solved according to the following algorithm.

Step 1. For each component, calculate the concentration $C_{i,j+1/2}$ at each position $x_i = i\Delta x$ ($i = 0, 1, 2, \ldots, n_s$) at time $t_{j+1/2} = t_j + 1/2\Delta t$ ($j = 0, 1, 2, \ldots, n_t$), where $t_j = \Sigma_{m=1}^{j} (\Delta t)_m$; Δx and Δt are, respectively, the discretized spatial and temporal increments, and n_t is the number of temporal increments. This is done by first determining the transported solution $C^{T}_{i,j+1/2}$ (no numerical diffusion), viz.

$$C^{T}_{i,j+\frac{1}{2}} = C_{i,j} - \frac{\Delta t}{2\Delta x}\left[v^{e}_{i+\frac{1}{2},j} C_{i+\frac{1}{2},j} - v^{e}_{i-\frac{1}{2},j} C_{i-\frac{1}{2},j} + f^{d}_{i+\frac{1}{2},j} - f^{d}_{i-\frac{1}{2},j} \right] \quad (12)$$

where the diffusive flux is

$$f^{d}_{i+\frac{1}{2},j} = -D\,\frac{(C_{i+1,j} - C_{i,j})}{\Delta x} \quad (13)$$

and $v^{e}_{i+1/2,j}$ and $C_{i+1/2,j}$ are calculated as the arithmetic average of the values at x_i and x_{i+1}. Next numerical diffusion is added to the transported solution to find $C^{D}_{i,j+1/2}$, i.e.

$$C^{D}_{i,j+\frac{1}{2}} = C^{T}_{i,j+\frac{1}{2}} - (g^{nd}_{i+\frac{1}{2},j} - g^{nd}_{i-\frac{1}{2},j}) \quad (14)$$

where

$$g^{nd}_{i+\frac{1}{2},j} = -\nu_{i+\frac{1}{2},j}(C_{i+1,j} - C_{i,j}) \quad (15)$$

has the form of a discretized diffusion flux multiplied by the ratio of the current time step to the spatial increment. $\nu_{i+1/2,j}$ is, in effect, a dimensionless velocity-dependent diffusion coefficient [18]

$$\nu_{i+\frac{1}{2},j} = \frac{1}{6} + \frac{1}{3}\left(\epsilon_{i+\frac{1}{2},j}\right)^2 \quad (16)$$

with

$$\epsilon_{i+\frac{1}{2},j} = \frac{\Delta t}{\Delta x} v^{e}_{i+\frac{1}{2},j} \quad (17)$$

Finally numerical antidiffusion is applied to find $C_{i,j+1/2}$, viz.

$$C_{i,j+\frac{1}{2}} = C^{D}_{i,j+\frac{1}{2}} - \left(g^{ad}_{i+\frac{1}{2},j} - g^{ad}_{i-\frac{1}{2},j} \right), \quad (18)$$

where

$$g^{ad}_{i+\frac{1}{2},j} = L\left\{ \mu_{i+\frac{1}{2},j}\left(C^{T}_{i+1,j+\frac{1}{2}} - C^{T}_{i,j+\frac{1}{2}}\right) \right\} \quad (19)$$

$$\mu_{i+\frac{1}{2},j} = \frac{1}{6} - \frac{1}{6}\left(\epsilon_{i+\frac{1}{2},j}\right)^2, \quad (20)$$

and $L\{g\}$ is the nonlinear function that applies the flux limiter to g. In the ZE and ITP simulations, the strong flux limiter described by Boris et al. [21] was applied, and that overall numerical scheme is identified here as PLPE1. This limiter prevents spurious overshoots and undershoots from forming by prohibiting the creation of new extrema, as well as the accentuation of existing extrema, during the antidiffusion stage. In the IEF simulation, two flux limiters were applied–the strong flux limiter of PLPE1 and a weaker limiter (cf. Eqs. (6–14), and (17–18) of Ref. [20]). The weaker flux limiter allows the creation and accentuation of extrema, as long as these extrema do not exceed the values of neighboring nodes from the previous time step. The scheme incorporating this flux limiter is identified here as PLPE2.

Step 2. For each component, calculate the concentration $C_{i,j+1}$ at time $t_{j+1} = t_j + \Delta t$. The step begins with a prediction of. the velocity $v^{e}_{i+1/2,j+1/2}$ and the flux $f^{d}_{i+1/2,j+1/2}$, which are calculated using the values of $C_{i,j+1/2}$ from Step 1 and Eqs. (2–5), (7–10), and (13). Next, as in Step 1, a transported solution $C^{T}_{i,j+1}$ is determined, viz.

$$C^{T}_{i,j+1} = C_{i,j} - \frac{\Delta t}{\Delta x}\left[v^{e}_{i+\frac{1}{2},j+\frac{1}{2}} C_{i+\frac{1}{2},j} - v^{e}_{i-\frac{1}{2},j+\frac{1}{2}} C_{i-\frac{1}{2},j} + f^{d}_{i+\frac{1}{2},j+\frac{1}{2}} - f^{d}_{i-\frac{1}{2},j+\frac{1}{2}} \right] \quad (21)$$

Numerical diffusion is then added to find $C^{D}_{i,j+1}$:

$$C^{D}_{i,j+1} = C^{D}_{i,j+1} - \left(g^{nd}_{i+\frac{1}{2},j+\frac{1}{2}} - g^{nd}_{i-\frac{1}{2},j+\frac{1}{2}} \right) \quad (22)$$

where

$$g^{nd}_{i+\frac{1}{2},j+\frac{1}{2}} = \nu_{i+\frac{1}{2},j+\frac{1}{2}}(C_{i+1,j} - C_{i,j}). \quad (23)$$

Lastly, numerical antidiffusion is applied to find:

$$C_{i,j+1} = C^{D}_{i,j+1} - \left(g^{ad}_{i+\frac{1}{2},j+\frac{1}{2}} - g^{ad}_{i-\frac{1}{2},j+\frac{1}{2}} \right) \quad (24)$$

where

$$g^{ad}_{i+\frac{1}{2},j+\frac{1}{2}} = L\left\{ \mu_{i+\frac{1}{2},j+\frac{1}{2}}(C^{T}_{i+1,j+1} - C^{T}_{i,j+1}) \right\} \quad (25)$$

Numerical implementation of the remainder of the model follows the method previously described by Palusinski et al. [4]. The second-order RK/FCT algorithm described above replaces the 5th-order Runge–Kutta–Fehlberg (RKF)/2nd-order Central Spatial Difference (CSD) algorithm used to solve Eqs. (6).

3.2. Explicit upwinding

To evaluate the performance of the PLPE FCT method for the transient electrophoretic separations model described in Section 2, three benchmark problems were solved, and the solutions compared to solutions derived from two other explicit numerical techniques. One was the RKF/CSD method described by Palusinski et al. [4]. This is a typical higher-order scheme that does not guarantee monotonicity, and includes the same spatial discretization as that used in the PLPE FCT algorithm to find the transported solution. The other method was an explicit first-order upwind scheme that guarantees monotonicity (at the expense of accuracy). These schemes were chosen for comparison to illustrate how FCT combines the second-order accuracy of the RKF/CSD method with the monotonicity of the first-order upwind methods. In the upwinding algorithm, the spatial discretization is equivalent to that in the first-order upwind schemes of Martens et al. [11], but the time derivative is discretized by a forward difference to yield a fully explicit scheme, as are the other schemes examined here. The second-order RK timestep used in the PLPE FCT algorithm is also used in the upwind scheme. The upwinding is done as follows:

For $v^{e}_{i,j} < 0$:

$$C_{i,j+\frac{1}{2}} = C_{i,j} - \frac{\Delta t}{2\Delta x}\left[v^{e}_{i+1,j} C_{i+1,j} - v^{e}_{i,j} C_{i,j} + f^{d}_{i+\frac{1}{2},j} - f^{d}_{i-\frac{1}{2},j} \right] \quad (26)$$

$$C_{i,j+1} = C_{i,j} - \frac{\Delta t}{\Delta x}\left[v^{e}_{i+1,j+\frac{1}{2}} C_{i+1,j} - v^{e}_{i,j+\frac{1}{2}} C_{i,j} + f^{d}_{i+\frac{1}{2},j+\frac{1}{2}} - f^{d}_{i-\frac{1}{2},j+\frac{1}{2}} \right] \quad (27)$$

For $v^{e}_{i,j} > 0$:

$$C_{i,j+\frac{1}{2}} = C_{i,j} - \frac{\Delta t}{2\Delta x}\left[v^{e}_{i,j}C_{i,j} - v^{e}_{i-1,j}C_{i-1,j} + f^{d}_{i+\frac{1}{2},j} - f^{d}_{i-\frac{1}{2},j}\right] \quad (28)$$

$$C_{i,j+1} = C_{i,j} - \frac{\Delta t}{\Delta x}\left[v^{e}_{i,j+\frac{1}{2}}C_{i,j} - v^{e}_{i-1,j+\frac{1}{2}}C_{i-1,j} + f^{d}_{i+\frac{1}{2},j+\frac{1}{2}} - f^{d}_{i-\frac{1}{2},j+\frac{1}{2}}\right] \quad (29)$$

This scheme is identified here as UPWIND, and the RKF/CSD method will henceforth be identified simply as CSD.

3.3. Discretization

In all simulations, the spatial discretization step was prescribed and the time step calculated to meet certain criteria specific to each numerical method. In the PLPE1 and PLPE2 simulations, the time step was calculated to maintain the maximum Courant number, $Co_{max} \equiv |\epsilon_{i,j}|_{max}$, at 0.45, since numerical monotonicity is only ensured using the PLPE method for $Co < 0.50$ [21]. Monotonicity for the UPWIND scheme however is guaranteed for $Co < 1.0$ [16], and thus Co was maintained at 0.90 for the upwind simulations. In the CSD simulations, the time step was controlled by the RKF algorithm, which adjusts the time step to maintain an estimate of the truncation error within prescribed bounds [28].

The spatial grid was prescribed to permit comparison to previously-published simulation results, and to establish the convergence requirements of each scheme. A reasonable definition of a converged solution might be a solution that changes everywhere by less than 1% of the full-scale value upon doubling the number of segments. However, at typical electric field strengths, component zone boundaries are often reduced to 0.01% of the column length or less. On a fixed uniform grid, a perfect numerical scheme, i.e. one that captures the entire zone boundary in one segment, would require at least 10 000 segments to correctly resolve such transitions, and hence meet the above defined convergence criterion. The numerical schemes studied here require at least 3 segments to converge in any zone boundary, and therefore even the best of these schemes would require an impractical amount of simulation time to meet this convergence requirement. Therefore, a converged solution is defined here as one which, upon doubling the number of segments, changes everywhere by less than 1% of the full-scale value, except in zone boundaries that are narrower than 0.2% of the column length. In these regions, the zone boundary thicknesses are required only to be resolved to 0.2% of the column length. The zone boundary thickness is defined here as the length over which a dependent variable's value changes from 1% to 99% of the value difference between one plateau value and another. These convergence criteria provide a reasonable basis for comparison of the numerical schemes delineated in this paper. Meeting more stringent convergence criteria efficiently would require the use of adaptive grids, which is beyond the scope of this paper.

3.4. Equipment

All simulations were performed on an IBM RISC System/6000 workstation, running the AIX Version 3.2 UNIX operating system and AIXwindows graphical user interface. All computations were coded in FORTRAN 77 and compiled using an AIX XL FORTRAN Compiler/6000 Version 2.3.

4. Results and discussion

4.1. ZE benchmark

A ZE separation of two weak bases, aniline and pyridine in a uniform buffer, was simulated using each of the numerical techniques described in Section 3. The buffer was composed of 12 m*M* Tris base and 20 m*M* acetic acid, and the analytes were introduced as a 5 mm sample plug, 5 mm from the anodic end of a 20 cm long capillary. Initial sample zone boundary thicknesses were approximately 4% of the zone width (~2 segments of fine mesh). The initial analyte concentrations in the sample plug were 1 m*M* each, and the detector was positioned 10 cm from the anode. The simulation was performed at a constant current density of 2547 A/m^2, which

corresponded to an initial potential difference of 6564 V applied across the column. In this separation process, the analytes are only an order of magnitude lower in concentration than the background buffer. As a result, the transport of the analytes is fully coupled with the transport of the buffer, and an electric field that is ultimately higher in the analyte zones than in the surrounding buffer generates selfsharpening leading edges of these zones. The sharp transitions advected at high Peclet numbers typically present problems for standard numerical techniques used for parabolic equations.

Computed electropherograms for this ZE separation are presented in Fig. 1. Panel (a) shows the electropherograms calculated using a relatively coarse grid spacing of $\Delta x = 0.05$ cm. The CSD solution is completely distorted by oscillations and the UPWIND solution produces peaks that are excessively eroded by numerical diffusion. This demonstrates the well known result that upwinding ensures monotonicity at the expense of significant numerical diffusion. The PLPE1 solution, however, produces peaks with no oscillations and much less numerical diffusion than the UPWIND scheme. The self-sharpening leading edges of the peaks remain remarkably vertical for such a coarse discretization; the boundary is spread over 2.4 s using the PLPE1 method, compared to 14 s with the UPWIND method. Also, the PLPE1 method resolves the peak heights to within 7% of the converged values (Fig. 1(b)), but the numerical spreading inherent in the UPWIND scheme has eroded the peaks by half. Numerical results of this separation on the same grid have previously been reported by Ermakov et al. [10], who found minor numerical oscillations at a current density of 509 A/m^2; at the current density simulated here, the Ermakov et al. solution was significantly distorted by numerical oscillations.

Additional electropherograms, calculated on a finer grid ($\Delta x = 0.01$ cm), for which the PLPE1 method has converged, are presented in Fig. 1(b). Again the CSD solution is marred by oscillations. The converged PLPE1 solution reveals that the shoulders on the peaks of the course grid are artifacts, probably resulting from the nonlinear behavior of the flux limiter [21]. The peaks generated by the UPWIND scheme are much closer to the converged PLPE1 solution, but the numerical diffusion has still eroded the peaks to the extent (14% error in peak heights) that the PLPE1 solution on the coarse grid (Fig. 1(a)) is closer to the converged solution (Fig. 1(b)). Table 1 lists the peak variances and relative errors in peak variance for PLPE1 and

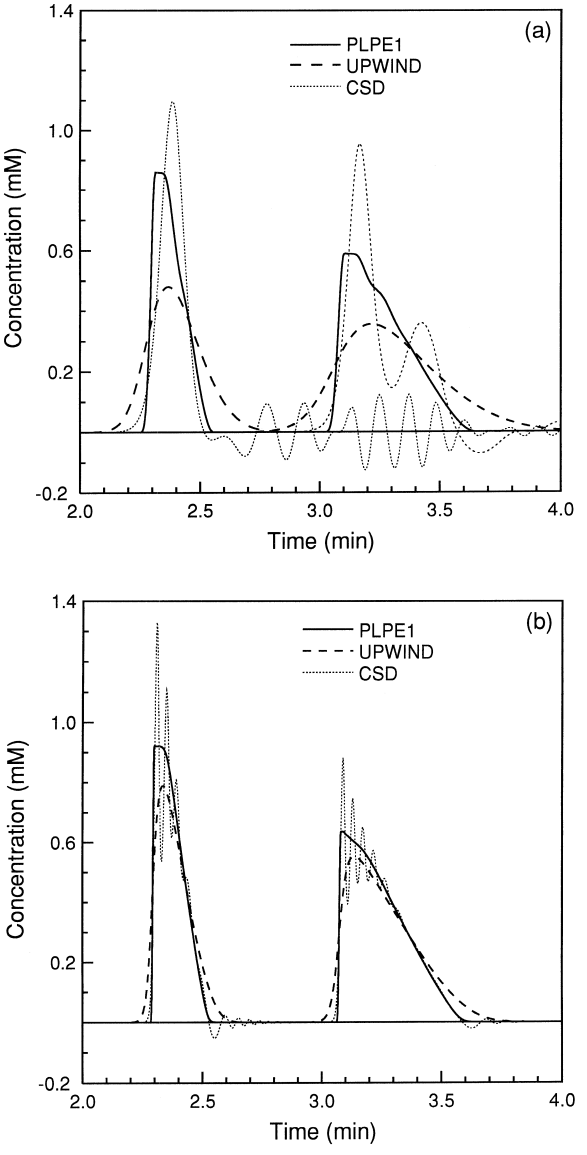

Fig. 1. ZE benchmark electropherograms. Pyridine is eluted first followed by aniline. Constant current, 2547 A/m^2; initial voltage, 6564 V across a 20 cm column. The detector is positioned at the center of the column. Initial buffer concentrations, 12 m*M* tris base/20 m*M* acetic acid; initial sample concentrations, 1 m*M* each. The grid spacing is (a) 0.05 cm and (b) 0.01 cm.

Table 1
ZE peak variances (σ^2) and relative errors in peak variance (ϵ)[a]

No. of segments	σ^2 (s^2)		$\%\epsilon$[b]	
	PLPE1	UPWIND	PLPE1	UPWIND
Aniline				
400	55.8	154.8	12.3	210.0
2000	*49.7*	70.9	0.0	42.7
Pyridine				
400	11.9	43.9	15.5	326.0
2000	*10.3*	16.8	0.0	63.1

[a] Italicized numbers indicate converged values.
[b] $\%\epsilon = 100\ (\sigma^2 - \text{Converged } \sigma^2)/(\text{Converged } \sigma^2)$.

UPWIND. CSD was not included in the Table because negative concentrations result in meaningless variances. Note that the relative errors of UPWIND on the *fine* grid are approximately five times those of PLPE1 on the *coarse* grid. Ikuta and Hirokawa reported simulating this separation on this grid, using an upwind scheme to obtain numerical stability [12]. Their upwind scheme suffered similarly from the deleterious effects of numerical diffusion.

A summary of the convergence requirements for each scheme is provided in Table 2. Using the PLPE1 method, a converged solution was realized in 24 min. The other methods however did not converge on a 10 000 segment grid that required almost 5 h of computation time. All simulation grids were limited to 10 000 segments, so the simulation time required for these 2 methods to converge was not determined.

The converged solution produced by the PLPE1 scheme shows the loss of peak resolution that can result from the coupling between the ion transport and the electric field. The flat tops of the converged peaks, particularly the pyridine peak, result from the complicated electric field that develops as the analytes separate in the first minute of separation. The presence of the analytes increases the conductivity, and thus lowers the electric field in the initial sample zone. This causes the basic buffer component to deplete, and the acidic component to accumulate on the leading edge of the sample zone. Because the pH is much closer to the pK of the acid than the pK of the base, the base has a much higher percent dissociation and thus a much higher effective mobility. As a result, the base depletes much faster than the acid accumulates in this region, causing an increase in the electric field. As the analytes migrate from the initial sample zone, they pass from a low-field region to a higher field region, and are also depleted. A decrease in analyte concentration reduces the depletion of the basic buffer on the leading edge of the analyte zones, which in turn slows the reduction in the analyte concentration. In this way, the concentrations are adjusted until separated analyte zones, lower in concentration than the original zone, are formed. These zones are essentially square because the initial zones are square, but because the basic buffer is depleted, the electric field is now higher in the analyte zones. This results in a self-sharpening leading edge and a broadening trailing edge. Thus a flat top of the analyte zone remains until the broadening edge spreads to the leading edge. The aniline zone is approximately at that stage as it passes the detector (Fig. 1(b)). The shapes of these peaks are not captured by the the UPWIND or CSD schemes, nor by any of the previously-published simulations of this ZE separation, because either numerical diffusion erodes or oscillations distort the profiles.

Table 2
Convergence requirements for ZE simulation

Scheme	Number of segments	Computation time (min)
PLPE1	2000	24
UPWIND	>10 000	>281
CSD	>10 000	>268

4.2. ITP benchmark

In an ITP separation, leading and terminating buffers are selected to establish an electric field that ultimately drives a train of sample and buffer zones to move isotachophoretically down the separation column. In accordance with the Kohlrausch condition [29], there are stepwise variations of the electric field in the direction of electrophoretic motion, and self-sharpening boundaries form between the zones where the net diffusive flux of each component is balanced by the net electromigrational flux (when observed from a frame of reference moving at the isotachophoretic velocity). At high electric Peclet numbers, i.e. high electric field

strengths, the zone boundaries must become extremely sharp to allow diffusion to balance the high electromigrational fluxes. This typically presents difficulties for numerical solutions.

To evaluate the performance of the PLPE method on an ITP calculation, an isotachophoretic separation of the two aforementioned weak base analytes was simulated. The leading electrolyte consisted of 18 m*M* sodium hydroxide and 20 m*M* acetic acid, and the terminating electrolyte was composed of 40 m*M* β-alanine and 50 m*M* acetic acid. Ten m*M* aniline and pyridine and 20 m*M* acetic acid were introduced as a 1 mm sample plug, 1 mm from the anodic end of a 40 mm long capillary. Initial zone boundary thicknesses were approximately 4% of the sample zone widths (~2 segments of fine mesh). A separation time of 42 s was simulated at a constant current of 2260 A/m^2, which corresponded to initial and final potential differences of 576 V and 3280 V, respectively, applied across the column.

The ITP simulation results of the 3 different methods are presented in Fig. 2, with the concentrations of the two sample zones bounded by the leading electrolyte on the right and the terminator on the left. Results are provided for the UPWIND and PLPE1 schemes on both coarse ($\Delta x = 50$ μm) and fine ($\Delta x = 13.3$ μm) grids; results of the CSD scheme are reported only on the fine grid because a solution could not be obtained on the coarse grid. Even on the fine grid, the CSD method computes zones that are greatly distorted by spurious oscillations. The PLPE1 solution on the fine grid, on the other hand, meets not only the convergence criteria defined in Section 3, but is also converged in the zone boundary between the two analytes. The PLPE1 and UPWIND schemes produce non-oscillatory solutions on each grid, but the zone boundaries calculated using the PLPE1 method are clearly sharper than those produced by the UPWIND scheme. The zone boundary thickness between the two analytes is plotted in Fig. 3 as a function of the grid spacing for the PLPE1 and UPWIND schemes. On the coarse grid, the UPWIND scheme predicts a boundary thickness that is more than six times larger than the 145 μm thickness predicted by the PLPE1 scheme. On the fine grid, the PLPE1 method converges on a thickness of 40 μm, as compared to 320 μm with the UPWIND method. In fact, the UPWIND method requires an order of magnitude smaller grid spacing just to resolve this zone boundary as well as the PLPE1 method does on the coarse grid. Numerical results of this separation have also been reported by Martens et al. using various implicit upwinding algorithms [11]; the method yielding the best overall simulation results (called DIME) predicted a zone boundary thickness of 120 μm on a mesh finer than that required of the PLPE1 method to convergence on the 40 μm boundary thickness. Numerical results of this separation on the coarse grid have also been reported by Ermakov et al. [10], who indicated that numerical oscillations form at a current density of 102 A/m^2. (Note that their results were obtained using a 1 cm sample plug and a grid spacing of 0.5 mm. Using those lengths and a current density of 2260 A/m^2, the PLPE1 method yielded a non-oscillatory solution, which was self-similar to that represented by the dashed line in Fig. 2(a)).

The convergence requirements for each method applied to the ITP simulation are summarized in Table 3. Again, both the UPWIND and CSD schemes did not converge at the limit of 10 000 segments, and thus would require several days to reach convergence. The PLPE1 method, however, converged in less than 9 h of simulation time.

4.3. IEF benchmark

IEF separations include some physics not relevant in ZE or ITP separations. In an IEF separation, amphoteric compounds migrate electrophoretically toward their isoelectric point (iep). As they approach their iep, their electromigrational velocities diminish, thus increasing the role of diffusion in their transport behavior. An IEF simulation thus provides a challenging test of a numerical scheme's ability to handle both diffusion and strong electromigration. This is particularly important as regards FCT, since it was first developed to solve unsteady convection problems with no physical diffusion. The character of each component balance (Eqs. (6)) in an IEF simulation is typically, at the outset, hyperbolic over the entire domain. With time, the components migrate toward their iep, where the component balance laws become locally parabolic. Most components approach their iep from either end of the separation domain, so the iep is a turning point in the com-

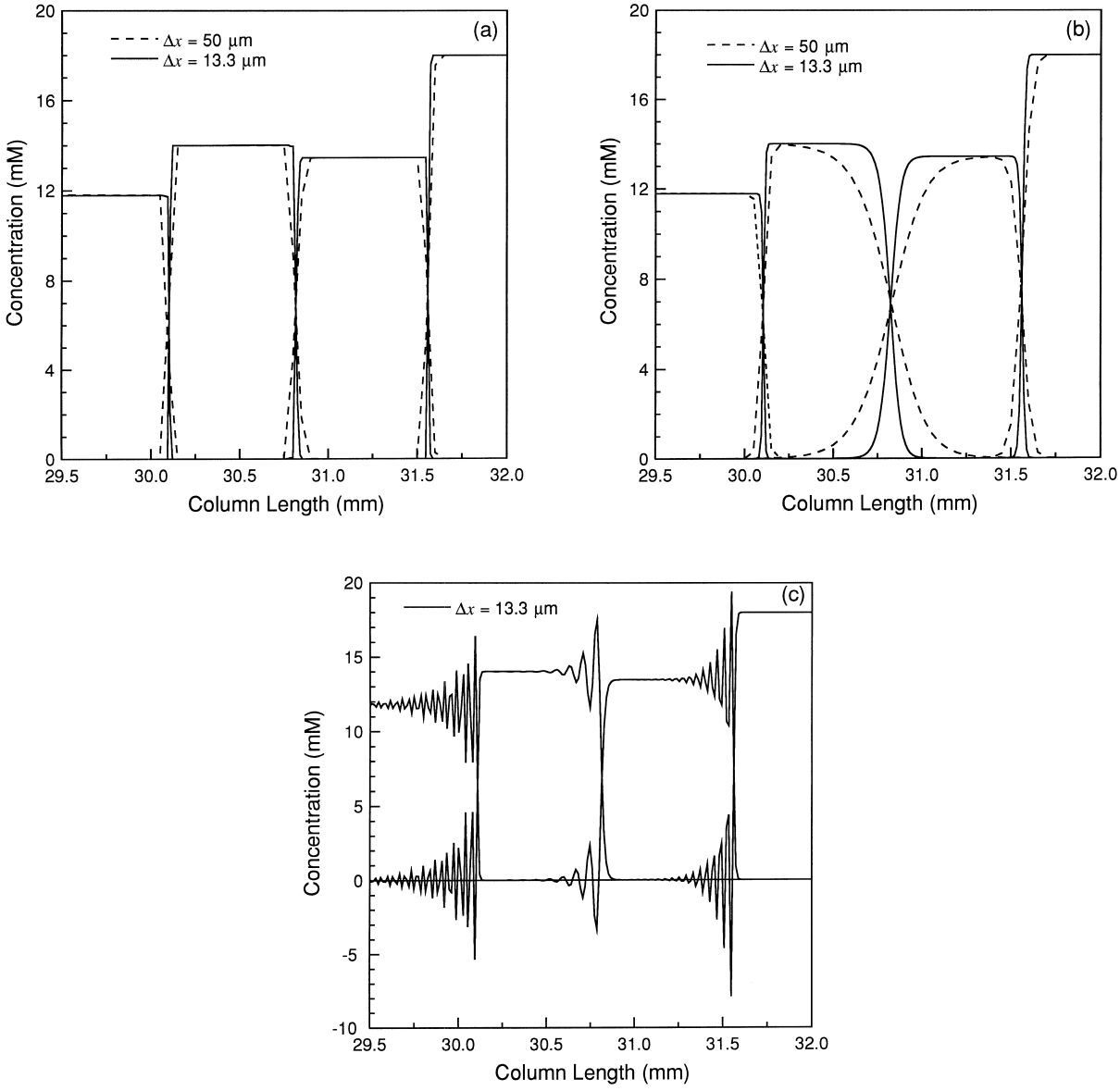

Fig. 2. ITP benchmark sample zone concentration profiles calculated by (a) PLPE1, (b) UPWIND, and (c) CSD. Constant current, 2260 A/m^2; initial voltage, 576 V across a 40 mm column. Initial concentrations: leader, 18 m*M* NaOH/20 m*M* HAc; terminator, 40 m*M* β-alanine/50 m*M* HAc; sample zone, 10 m*M* aniline and pyridine in 20 m*M* HAc. The terminating electrolyte zone is to the left, followed by aniline, pyridine, and the leading electrolyte zone to the right. Anode to the left.

ponent balance law. A numerical scheme applied to an IEF separation must therefore handle the dual hyperbolic/parabolic character of the balance laws, as well as the turning point at the iep.

To evaluate the PLPE1 method for IEF, the focusing of a protein in a natural pH gradient generated by 3 amino acids was simulated. A constant 96.2 V (initial current density 500 A/m^2) potential difference was applied across a 1 cm separation domain with no-flux boundary conditions at the ends. The initial uniform concentrations of components were 10 m*M* each of glutamic acid,

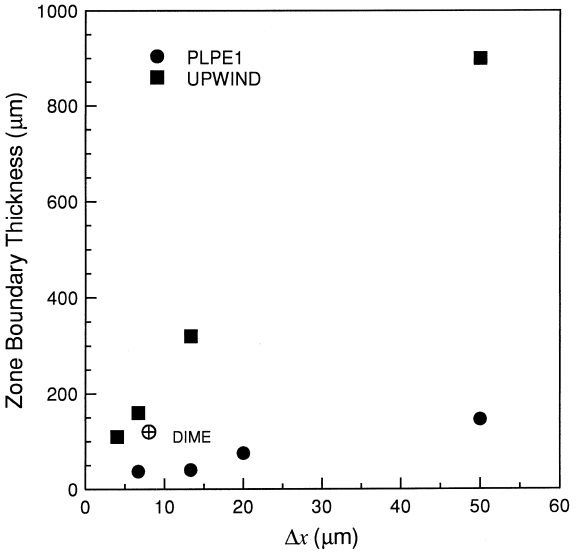

Fig. 3. Predicted ITP steady state boundary thickness between the aniline and pyridine zones as a function of the spatial grid size. The boundary thickness quoted is defined as the distance over which the zone concentrations change from 1% to 99% of their plateau values. Simulation conditions are as for Fig. 2. The DIME data point is from page 56 of Martens et al. [11].

cycloserine, and arginine, and 7.5 μ*M* of bovine serum albumin (BSA). The protein was focused for one min. Results of this simulation conducted at constant current were presented by Mosher et al. for current densities two orders of magnitude lower (for longer times) [5]. Their results show a relatively broad BSA peak occupying approximately 5% to 10% of the simulation domain and similarly broad boundaries between the carrier ampholyte zones. As shown in Figs. 4 and 5, the ampholyte boundaries and the BSA peak are much sharper at the higher field strength.

Fig. 4 shows the carrier ampholyte concentrations computed on coarse ($\Delta x = 20$ μm) and fine ($\Delta x = 3.33$ μm) grids with each numerical technique. As in the ITP simulation, the CSD method would not generate a solution on the coarse grid. The differences between the PLPE1 solutions for the carrier ampholyte concentrations on the coarse and fine

Table 3
Convergence requirements for ITP simulation

	Number of segments	Computation time (h)
PLPE1	3000	8.6
UPWIND	>10 000	>47.5
CSD	>10 000	>33.5

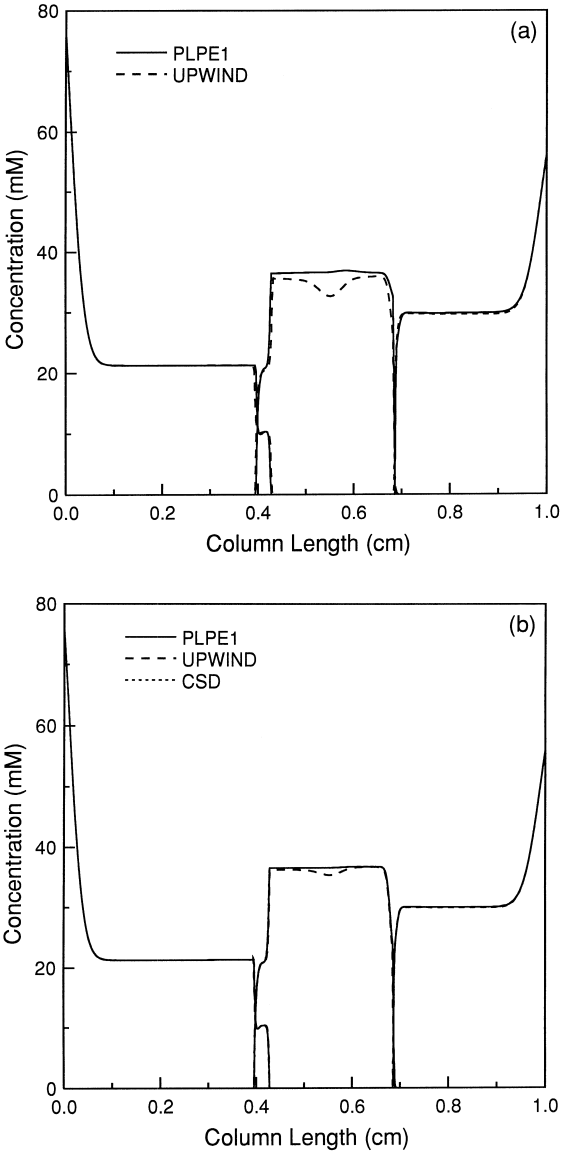

Fig. 4. IEF benchmark carrier ampholyte concentration profiles. The zone on the left boundary is glutamic acid, followed by cycloserine in the center, and the arginine zone on the right boundary. Constant voltage, 96.2 V across a 1 cm column; initial current density, 500 A/m^2. Initial carrier ampholyte concentrations, 10 m*M* each; initial BSA concentration 7.5 μ*M*. The grid spacing is (a) 20 μm and (b) 3.33 μm. Anode to the left.

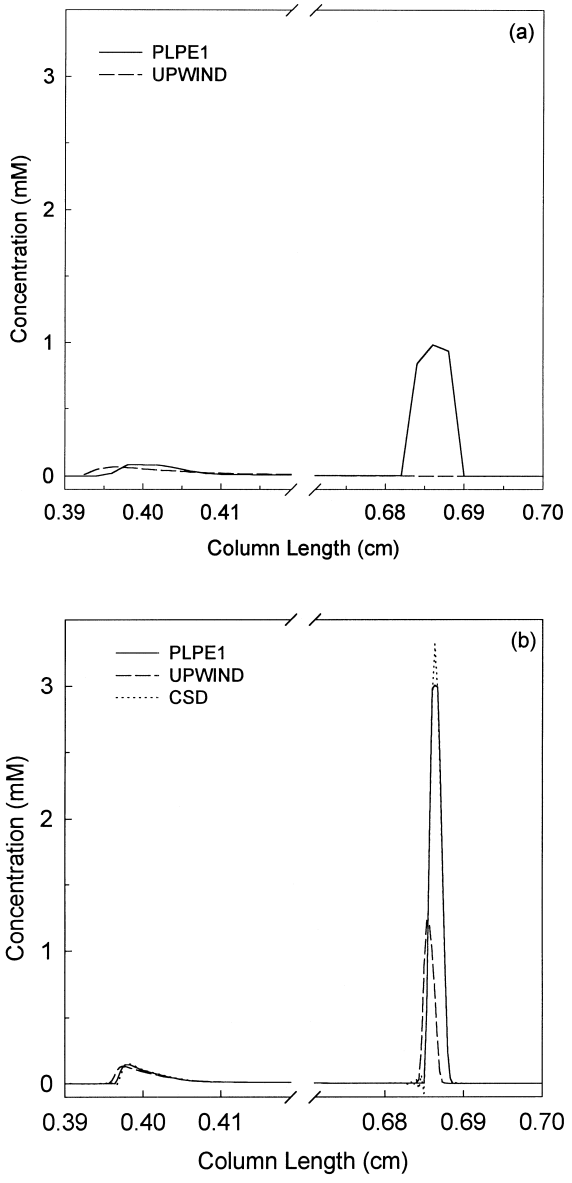

Fig. 5. IEF benchmark BSA concentration profiles. Simulation conditions are as for Fig. 4. The grid spacing is (a) 20 μm and (b) 3.33 μm. Note: results are interpolated linearly between grid points.

grids are barely perceptible on the column length scale, indicating that these components are nearly converged on the coarse grid. The UPWIND solution on the coarse grid exhibits a bit more numerical diffusion, and, more importantly, is flawed with respect to the cycloserine zone concentration. This results from a mass balance error that occurs where the electrophoretic velocity changes sign (the turning point). The UPWIND scheme approximates the electromigrational derivative at such a point by a forward difference at a node where the velocity is negative and by a backward difference at an adjacent node where the velocity is positive. This results in an inconsistency in the representation of the mass flux for the segments adjacent to the iep. With a sufficiently fine grid, the velocity at these neighboring nodes will approach zero, making the finite difference representation at the turning point irrelevant, and the mass balance error will vanish. On the grids used here, the mass balance error is sufficient to affect the computed concentration field. No such errors occur in the arginine and glutamic acid zones because they accumulate on the ends of the column in approach to their iep, and thus are either positive or negative over the entire simulation domain. On the fine grid, the cycloserine mass balance error is reduced from 4.8% to 1.5%, and a reduction in the zone concentration error is observed. Except for the UPWIND results in the cylcoserine zone, the carrier ampholyte concentrations of all three schemes are indistinguishable for the fine grid on the column length scale (Fig. 4(b)).

The protein concentration field is shown in Fig. 5. The separation has not quite reached steady state, as a smaller cathodic peak is migrating toward the anodic peak at the BSA iep. The effect of numerical diffusion on the UPWIND solution on the coarse grid (Fig. 5(a)) can be observed in the small cathodic peak, and mass balance errors by the UPWIND method have completely eliminated the focused protein peak. The BSA mass balance error is far worse than that for cycloserine because the BSA zone is narrow, and thus the BSA electromigrational velocity changes from a significant positive velocity to a significant negative velocity over a short interval. On the fine grid (Fig. 5(b)), the BSA mass balance error is reduced from 74% to 48%, and the focused peak is partially recovered. The PLPE1 solution on the coarse grid accurately predicts the position of the focused protein peak, but the peak height and width change dramatically when calculated on the fine grid. This is not so much a result of numerical diffusion as it is a simple matter of resolution. The BSA zone width predicted on the fine

grid was 30 μm, which is just slightly wider than the 20 μm segment width of the coarse grid. Therefore, even an ideal numerical scheme, which would require 2 segments to resolve a peak positioned with its apex at a node, could not properly resolve the BSA peak on the coarse grid. The PLPE1 solution on the fine grid (Fig. 5(b)) meets all the convergence criteria defined in Section 3 except that the BSA peak concentration changed by more than 1% upon doubling the number of segments. It was estimated that at least a week of simulation time would be required to establish the convergence grid. To converge on the narrow BSA zone with a uniform grid would be inefficient, since computation time would be wasted on thousands of nodes where the concentration would be virtually constant on the segment length scale.

Fig. 5(b) also reveals that the CSD solution for the protein concentration field includes a few small oscillations on the left edge of the focused peak, but this method resolves the peak slightly better than the PLPE1 method. The characteristic 3-node flat top of the PLPE1-generated peak indicates that this results from the 'clipping' phenomenon [20,21], common to flux limiter techniques. The clipping in this case is caused by the strong antidiffusion flux limiter, which does not allow numerical antidiffusion to push the concentration of the peak node above that of neighboring nodes. Fig. 6 shows the BSA peak calculated using the more relaxed flux limiter in the PLPE2 method. With this method, the peak is resolved as well as with CSD method, and no oscillations are formed. Furthermore, this improvement is realized at an insignificant computational cost (4% increase in simulation time), because approximately 80% of the total simulation time is devoted to solving the nonlinear algebraic system of equations governing the pH and component species concentrations. Applying the PLPE2 method, the BSA peak concentration predicted on the fine grid changes by less than 5% upon doubling the number of nodes on this grid.

Fig. 7 shows the pH, conductivity, and electric field computed for this IEF separation on the fine grid using the PLPE2, CSD, and UPWIND schemes. The three methods yield essentially indistinguishable conductivity and pH profiles on the column length scale, as they did for the concentration of the carrier ampholytes. Small pH oscillations on the order of 0.1 unit, barely visible on this scale, are produced by the CSD method. The CSD method generates substantial oscillations in the electric field (20–30 V/cm amplitude) near the carrier ampholyte zone boundaries. The UPWIND-generated electric field also deviates in the cycloserine zone as a result of the mass balance error.

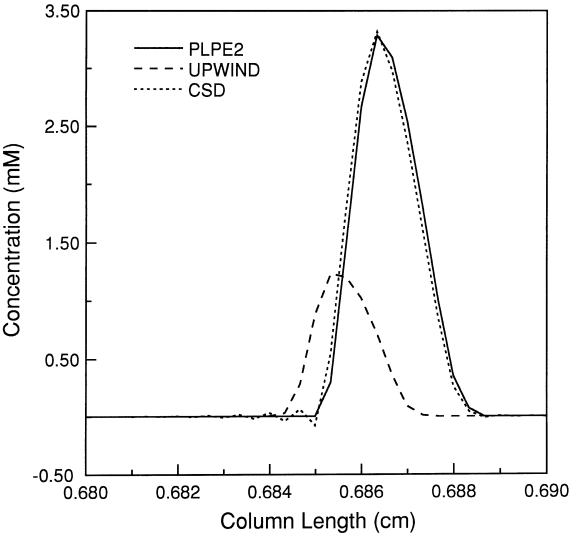

Fig. 6. Improved resolution of the focused BSA peak by the PLPE2 method. Simulation conditions are as for Fig. 4(b). Note: results are interpolated linearly between grid points.

5. Conclusions

The FCT finite difference scheme is an effective method for solving the coupled set of unsteady electromigration–diffusion equations in the electrophoretic separations model. The FCT method yields second-order solutions to these equations, and prevents the formation of numerical oscillations. In contrast to uncorrected higher-order difference schemes, and the artificial dispersion scheme presented by Ermakov et al. [10], there is essentially no Peclet number limit on the stability nor the monotonicity of FCT [15–21]. At $Pe_L > O(10^3)$, converged solutions using FCT can typically be realized on coarser grids and in significantly less simulation time than the UPWIND or CSD methods. Also, for the benchmark separations simulated here, the PLPE

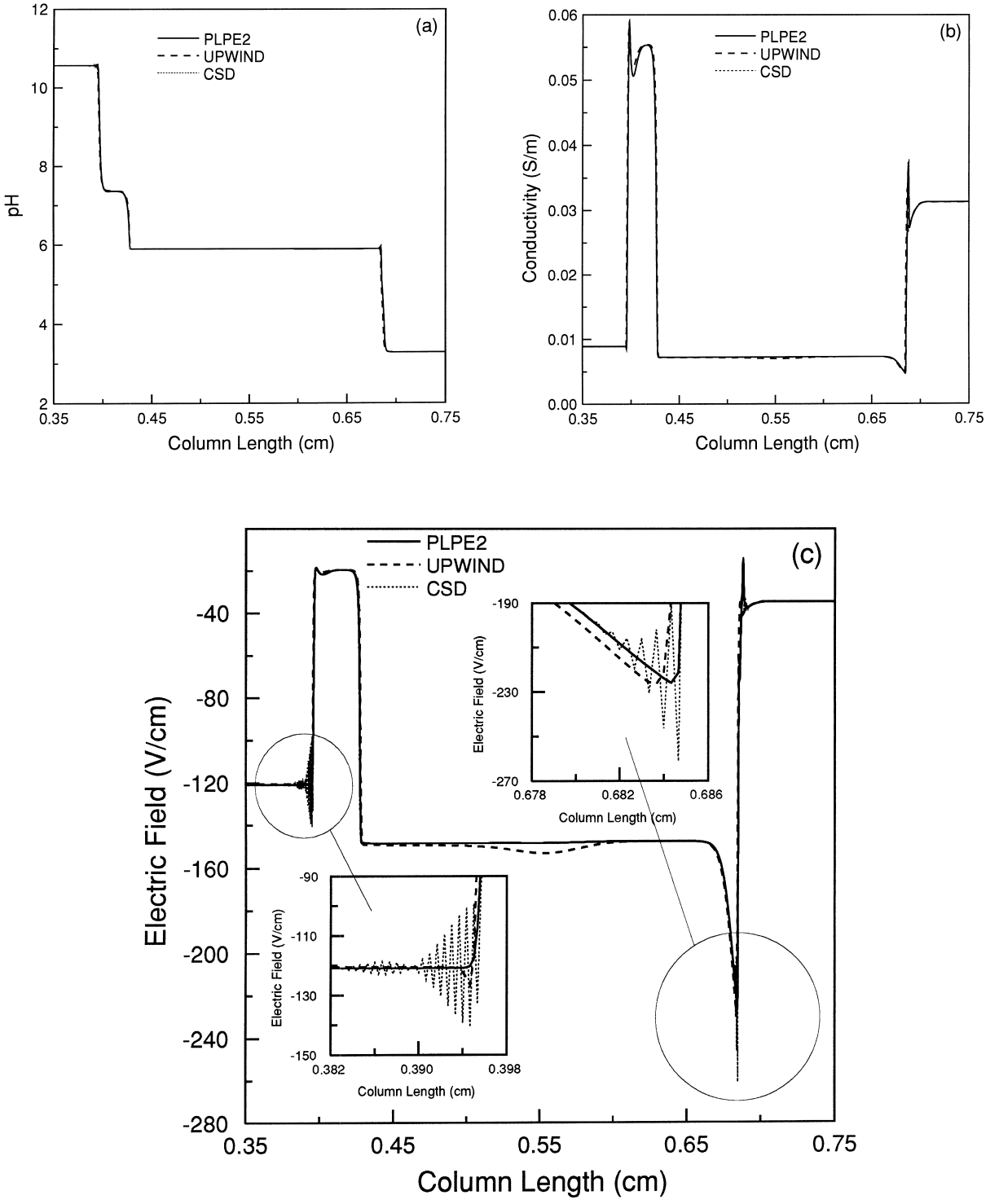

Fig. 7. IEF benchmark pH, conductivity, and electric field profiles. Simulation conditions are as for Fig. 4(b).

method yielded non-oscillatory and significantly more accurate solutions to the electrophoresis model than any of the other published methods. This improved efficiency and the explicit structure of the algorithm will become even more important for two and three dimensional unsteady electrophoresis problems, wherein the simulation time scales as n_s^2 and n_s^4 respectively.

In cases such as the IEF benchmark, where convergence was limited by the resolution of the narrow but stationary protein peak, FCT provides only a modest improvement over the CSD method. In no cases studied to date has the FCT method required a finer grid than either the UPWIND or CSD methods; moreover, on coarse grids where CSD fails, one can still use FCT to obtain non-converged solutions that yield such gross features as the position and approximate shape of zone boundaries or peaks.

Finally, for problems such as the IEF benchmark, which are characterized by a disparity in length scales, an adaptive mesh should be developed to provide converged solutions with reasonable efficiency. When combined with an adaptive mesh, the FCT scheme will greatly reduce the number of segments required to converge in regions where sharp gradients are advected at high electric Peclet numbers.

Acknowledgements

This work was supported, in part, by the NSF/SRC Center for Environmentally-Benign Semiconductor Manufacturing at The University of Arizona.

References

[1] R. Kniss, Am. Lab. 30 (1998) 40.
[2] M. Bier, O.A. Palusinski, R.A. Mosher, D.A. Saville, Science 219 (1983) 1281.
[3] D.A. Saville, O.A. Palusinski, AIChE J. 32 (1986) 207.
[4] O.A. Palusinski, A. Graham, R.A. Mosher, M. Bier, D.A. Saville, AIChE J. 32 (1986) 215.
[5] R.A. Mosher, D.A. Saville, XV. Thormann, The Dynamics of Electrophoresis, VCH, Weinhem, 1992.
[6] E.V. Dose, G.A. Guiochon, Anal. Chem. 63 (1991) 1063.
[7] C. Schafer-Nielsen, Electrophoresis 16 (1995) 1369.
[8] C. Schwer, B. Gas, F. Lottspeich, E. Kenndler, Anal. Chem. 65 (1993) 2108.
[9] S.V. Ermakov, O.S. Mazhorova, Yu.P. Popov, Informatica 3 (1992) 173.
[10] S.V. Ermakov, M.S. Bello, P.G. Righetti, J. Chromatogr. A 661 (1994) 265.
[11] J.H.P.A. Martens, J.C. Reijenga, J.H.M. ten Thije Boonkkamp, R.M.M. Mattheij, F.M. Everaerts, J. Chromatogr. A 772 (1997) 49.
[12] N. Ikuta, T. Hirokawa, J. Chromatogr. A 802 (1998) 49.
[13] P.K. Sweby, SIAM J. Numer. Anal. 21 (1984) 995.
[14] B. van Leer, J. Comp. Phys. 14 (1974) 361.
[15] J.P. Boris, D.L. Book, J. Comp. Phys. 11 (1973) 38.
[16] D.L. Book, J.P. Boris, K. Ham, J. Comp. Phys. 18 (1975) 248.
[17] J.P. Boris, D.L. Book, J. Comp. Phys. 20 (1976) 397.
[18] J.P. Boris, D.L. Book, Methods in Computational Physics 16 (1976) 85.
[19] D.L. Book, J.P. Boris, S.T. Zalesak, in: D.L. Book (Ed.), Finite-Difference Techniques for Vectorized Fluid Dynamics Calculations, New York, 1981, Chapter 3, p. 29.
[20] S.T. Zalesak, J. Comp. Phys. 31 (1979) 335.
[21] J.P. Boris, A.M. Landsberg, E.S. Oran, J.H. Gardner, LCPFCT – Flux-Corrected Transport Algorithm for Solving Generalized Continuity Equations, NRL Memorandum Report 6410-93-7192, Naval Research Laboratory, Washington, 1993.
[22] D. Odstrcil, J. Comp. Phys. 91 (1990) 71.
[23] N. Grandjouan, J. Comp. Phys. 91 (1990) 424.
[24] M.J. Clifton, Electrophoresis 14 (1993) 1284.
[25] S. Blanco, M.J. Clifton, J.L. Joly, G. Peltre, Electrophoresis 17 (1996) 1126.
[26] J.L. Anderson, W.K. Idol, Chem. Eng. Commun. 38 (1985) 93.
[27] R.A. Mosher, C.X. Zhang, J. Caslavska, W. Thormann, J. Chromatogr. A 716 (1995) 17.
[28] H.A. Watts, Trans. Soc. Computer Simulation 1 (1985) 15.
[29] F. Kohlrausch, Ann. Phys. 62 (1897) 209.